

# Enhanced Ferromagnetism in Monolayer $\text{Cr}_2\text{Te}_3$ via Topological Insulator Coupling

Yunbo Ou,<sup>1,\*</sup> Murod Mirzhalilov,<sup>2</sup> Norbert M. Nemes,<sup>3</sup> Jose L. Martinez,<sup>4</sup> Mirko Rocci,<sup>1</sup> Austin Akey,<sup>5</sup> Wenbo Ge,<sup>6</sup> Dhavala Suri,<sup>7</sup> Yiping Wang,<sup>8</sup> Haile Ambaye,<sup>9</sup> Jong Keum,<sup>9,10</sup> Mohit Randeria,<sup>2</sup> Nandini Trivedi,<sup>2</sup> Kenneth S. Burch,<sup>8</sup> David C. Bell,<sup>5</sup> Weida Wu,<sup>6</sup> Don Heiman,<sup>1,11</sup> Valeria Lauter,<sup>9</sup> Jagadeesh S. Moodera,<sup>1,12,†</sup> and Hang Chi<sup>1,13,14,‡</sup>

<sup>1</sup>*Francis Bitter Magnet Laboratory, Plasma Science and Fusion Center, Massachusetts Institute of Technology, Cambridge, Massachusetts 02139, USA*

<sup>2</sup>*Department of Physics, The Ohio State University, Columbus, Ohio 43210, USA*

<sup>3</sup>*GFMC, Departamento Física de Materiales. Facultad de Ciencias Físicas, Universidad Complutense de Madrid, 28040, Madrid, Spain*

<sup>4</sup>*Instituto de Ciencia de Materiales de Madrid ICM-CONIC, Calle Sor Juana Inés de la Cruz, 3, Cantoblanco, Madrid 28049, Spain*

<sup>5</sup>*Center for Nanoscale Systems, Harvard University, Massachusetts 02139, USA*

<sup>6</sup>*Department of Physics and Astronomy, Rutgers University, Piscataway, New Jersey 08854, USA*

<sup>7</sup>*Centre for Nano Science and Engineering, Indian Institute of Science, Bengaluru, Karnataka 560012, India*

<sup>8</sup>*Department of Physics, Boston College, Chestnut Hill, Massachusetts 02467, USA*

<sup>9</sup>*Neutron Scattering Division, Neutron Sciences Directorate, Oak Ridge National Laboratory, Oak Ridge, Tennessee 37831, USA*

<sup>10</sup>*Center for Nanophase Materials Sciences, Physical Science Directorate, Oak Ridge National Laboratory, Oak Ridge, Tennessee 37831, USA*

<sup>11</sup>*Department of Physics, Northeastern University, Boston, Massachusetts 02115, USA*

<sup>12</sup>*Department of Physics, Massachusetts Institute of Technology, Cambridge, Massachusetts 02139, USA*

<sup>13</sup>*Department of Physics, University of Ottawa, Ottawa, Ontario K1N 6N5, Canada*

<sup>14</sup>*Nexus for Quantum Technologies, University of Ottawa, Ottawa, Ontario, K1N 6N5, Canada*

(Dated: December 27, 2023)

Exchange-coupled interfaces are pivotal in exploiting two-dimensional (2D) ferromagnetism. Due to the extraordinary correlations among charge, spin, orbital and lattice degrees of freedom, layered magnetic transition metal chalcogenides (TMCs) bode well for exotic topological phenomena. Here we report the realization of wafer-scale  $\text{Cr}_2\text{Te}_3$  down to monolayer (ML) on insulating  $\text{SrTiO}_3(111)$  substrates using molecular beam epitaxy. Robust ferromagnetism emerges in 2D  $\text{Cr}_2\text{Te}_3$  ML with a Curie temperature  $T_C = 17$  K. Moreover, when  $\text{Cr}_2\text{Te}_3$  is proximitized with topological insulator (TI)  $(\text{Bi,Sb})_2\text{Te}_3$ , the magnetism becomes stronger – for 1 ML,  $T_C$  increases to 30 K, while for 2 ML it boosts from 65 K to 82 K. Our experiments and theory strongly indicate that the Bloembergen-Rowland interaction is likely a universal aspect of  $T_C$  enhancement in TI-coupled magnetic heterostructures. The topological-surface-enhanced magnetism in 2D TMC enables further exchange coupling physics and quantum hybrid studies, including paving the way to realize interface-modulated topological electronics.

Magnetism has been at the center of modern information technologies involving sensor, memory and logic devices [1]. Recent development of monolayer (ML) van der Waals (vdW) magnetic materials [2–5], such as  $\text{FePS}_3$ ,  $\text{CrI}_3$ ,  $\text{Cr}_2\text{Ge}_2\text{Te}_6$ ,  $\text{Fe}_3\text{GeTe}_2$ ,  $\text{VSe}_2$ ,  $\text{MnSe}_x$ ,  $\text{CrSBr}$  and  $\text{AgCrP}_2\text{S}_6$ , have revealed the feasibility of exploiting long-range order and magnetic defects for quantum information storage and processing [6–14]. Utilizing novel vdW magnets, many appealing properties of topological materials, such as large anomalous Hall effect (AHE), topological Hall effect and spin-filtered tunneling effect have been demonstrated [15–17]. Nonetheless, wafer-size ML magnets on insulating substrates, favoring scalability for practical applications, are still much desired.

Among various systems of magnetic transition metal chalcogenides (TMCs), chromium telluride ( $\text{Cr}_2\text{Te}_3$ ) thin films are particularly well suited for exploring magnetism towards the ML regime due to its unique crystalline, electronic and magnetic structures [18, 19]. Furthermore,

the structural and chemical compatibility allows versatile interfacial modulation, leveraging the salient surface properties when hybridized with  $\text{Bi}_2\text{Te}_3$ -based topological insulators (TIs) [20].

As shown in Fig. 1a,  $\text{Cr}_2\text{Te}_3$  crystallizes in a  $P\bar{3}1c$  ( $D_{3d}^2$ , No. 163) structure with perpendicular magnetic anisotropy (PMA) along the crystallographic  $c$  axis and a bulk Curie temperature  $T_C$  of  $\sim 180$  K [21]. Along the  $c$  axis,  $\text{Cr}_2\text{Te}_3$  is composed of alternatively stacked (i) ferromagnetic Te-Cr1(Cr2)-Te lamellae similar to those in  $\text{CrTe}_2$  [22–25] and (ii) weakly antiferromagnetic Cr3 layers [26] with a larger intra-layer Cr-Cr distance and often partial occupancy [18]. It can thus be regarded as a quasi-two-dimensional (2D) system [27], and we herein designate the Te-Cr1(Cr2)-Te-Cr3 configuration as a ML.

Here we report the growth of high quality  $\text{Cr}_2\text{Te}_3$  thin films on insulating  $\text{SrTiO}_3(111)$  substrates using molecular beam epitaxy (MBE). Incorporating structural, magnetic and transport measurements, we

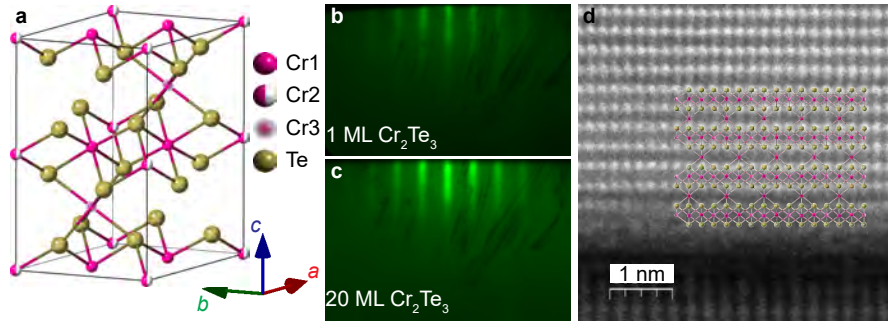


**Figure 1 | Structure of  $\text{Cr}_2\text{Te}_3$  thin films.** **a** Atomic structure of  $\text{Cr}_2\text{Te}_3$ , where three different Cr atoms are labeled as Cr1, Cr2, and Cr3, respectively. **b-c** RHEED patterns along the  $[100]$  direction of  $\text{Cr}_2\text{Te}_3$ , for 1 ML (**b**) and 20 ML (**c**)  $\text{Cr}_2\text{Te}_3$  films grown on  $\text{SrTiO}_3(111)$ , respectively. **d** HRSTEM HAADF image of  $\text{Cr}_2\text{Te}_3$  on  $\text{SrTiO}_3$  for the  $(100)$  plane.

have demonstrated that the ferromagnetism in  $\text{Cr}_2\text{Te}_3$  prevails down to 1 ML. The ordering strength in turn is amplified by exchange coupling to a TI, leading to an increased  $T_C$ . Our theoretical modeling further corroborates that topological surface states of TI are effective in stabilizing interfacial spin textures with boosted magnetic ordering, serving as a *general* strategy for enhancing  $T_C$  in 2D vdW magnetic systems.

### Structure and physical properties.

$\text{Cr}_2\text{Te}_3$  films were grown on insulating  $\text{SrTiO}_3(111)$  substrates. The streaky *in situ* reflection high energy electron diffraction (RHEED) patterns shown in Fig. 1b,c indicate the 2D layered growth of the films down to 1 ML. The typical X-ray diffraction (XRD) patterns (shown in Supplementary Fig. 1) reveal good crystallinity of  $\text{Cr}_2\text{Te}_3$  films on  $\text{SrTiO}_3(111)$  substrates and are consistent with previously reported  $\text{Cr}_2\text{Te}_3$  results [18, 28, 29]. The bulk (for film with thickness  $t = 100$  ML) lattice constants were obtained as  $a_{\text{XRD}} = 6.686 (\pm 0.007)$  Å and  $c_{\text{XRD}} = 12.164 (\pm 0.003)$  Å.

A sharp and flat interface between the film and the substrate is evident, as illustrated in the high-resolution scanning transmission electron microscopy (HRSTEM) high-angle annular dark-field (HAADF) image (Fig. 1d and Supplementary Fig. 2). The well-resolved region with darker contrast between Te-Cr1(Cr2)-Te trilayers corresponds to the Cr3 sites. The Raman spectra are found to display at least six phonon peaks that are independent of the polarization angle with respect to the crystal axes, consistent with the  $\text{Cr}_2\text{Te}_3$  phase (Supplementary Fig. 3) [30]. Measurements were performed on multiple spots across the film to verify the long-range uniformity (as also seen in magnetic force microscopy in Supplementary Fig. 3).

The thickness- and temperature-dependent longitudinal electrical resistivity  $\rho_{xx}(T)$  of  $\text{Cr}_2\text{Te}_3$  reveal that thick ( $t = 100$  ML)  $\text{Cr}_2\text{Te}_3$  film is metallic at ambient temperature and displays a metal-insulator transition (MIT) like behavior at  $T_{\text{MIT}} = 8$  K (Fig. 2a). The inflec-

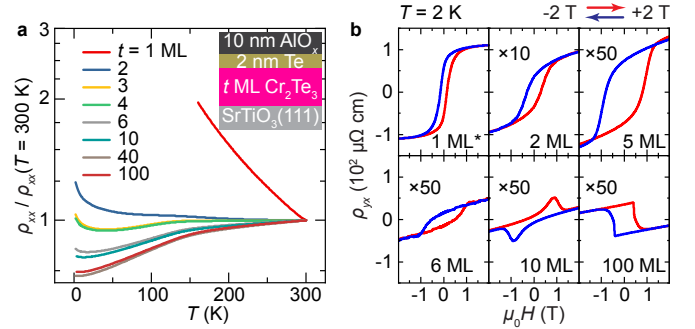


**Figure 2 | Transport properties of  $\text{Cr}_2\text{Te}_3$  thin films.** **a** Longitudinal electrical resistivity  $\rho_{xx}$  normalized to values at 300 K of  $\text{Cr}_2\text{Te}_3$  films with thickness  $t = 1 - 100$  ML. The inset is the schematic film structure. **b** The Hall traces  $\rho_{yx}$  of  $\text{Cr}_2\text{Te}_3$  films with selected  $t = 1 - 100$  ML at 2 K. The 1 ML\* data were taken from 4 QL  $(\text{Bi,Sb})_2\text{Te}_3/1$  ML  $\text{Cr}_2\text{Te}_3/\text{SrTiO}_3(111)$ . For better visibility, data for 2 ML and 5 - 100 ML were magnified  $\times 10$  and  $\times 50$ , respectively.

tion point increases logarithmically at reduced thickness and exceeds 300 K for  $t = 1$  and 2 ML. Moreover, upon reducing thickness,  $\rho_{xx}$  at room temperature increases in magnitude (see Supplementary Fig. 4). Since it becomes too insulating to measure at low temperature, for the Hall experiments (Fig. 2b), the signal for  $t = 1$  ML was collected by probing the transport in a proximitized TI of 4 quintuple layer (QL)  $(\text{Bi}_{0.23}\text{Sb}_{0.77})_2\text{Te}_3$  (BST) on top (labeled as 1 ML\*).

The clear AHE hysteresis in the Hall resistivity  $\rho_{yx}(H)$  for all  $t$  ranging from 1 to 100 ML, with magnetic field  $H$  applied perpendicular to the  $ab$  basal plane, unambiguously demonstrates the existence of ferromagnetism all the way down to 1 ML. The hysteresis in  $\rho_{yx}(H)$  originates from the magnetization  $M(H)$  of  $\text{Cr}_2\text{Te}_3$ . The remanent magnetization and/or Hall resistivity at zero field attest to the long-range ferromagnetic order, which disappears upon warming above  $T_C$ .

At the lowest measured  $T = 2$  K, while the anomalous

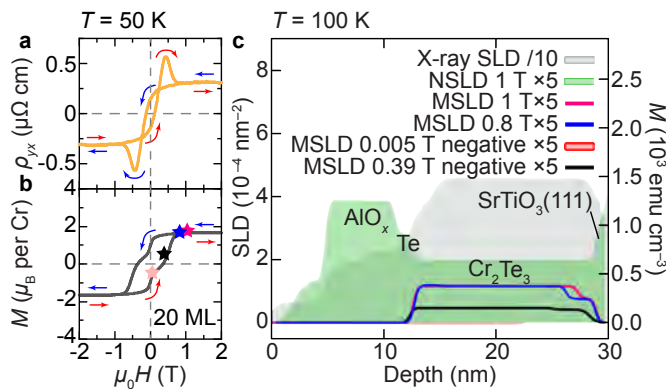


**Figure 3 | Magnetic properties of  $\text{Cr}_2\text{Te}_3$  thin films.** **a** Two-component characteristics of the field-dependent anomalous Hall resistivity  $\rho_{yx}$  and **b** out-of-plane magnetization  $M$  for  $t = 20$  ML at 50 K, as corroborated by **c** the depth profiles of X-ray, PNR nuclear (NSLD) and magnetic (MSLD) scattering length densities (SLD) for  $t = 26$  ML at 100 K. The MSLD data were collected at in-plane field 1 T, 0.8 T, then 0.005 T and 0.39 T (marked as “negative”, meaning after a negative saturation at  $-1$  T), corresponding to the typical locations labeled by the asterisks in the hysteresis loop in **b**. The arrows in **a-b** depict the field sweeping directions.

Hall resistivity  $\rho_{yx}^{\text{AH}}$  (defined as the zero field  $\rho_{yx}$  value after fully saturated at positive  $H$ ) is positive for the thinnest films, it changes sign to negative for  $t > 6$  ML, while the ordinary Hall effect forming the linear background maintains the same positive sign for all  $t$ . In addition, for intermediate thicknesses, e.g.,  $t = 6, 10$  (Fig. 2b) and 20 ML (Fig. 3a),  $\rho_{yx}(H)$  develops a notable hump feature at around the coercive field  $H_c$  during the magnetic moment reversal process. Further increase in thickness renders bulk dominating over interface effects, recovering a square-like hysteresis in  $\rho_{yx}(H)$  for  $t = 100$  ML. The manifestation of AHE sign reversal, hump-shaped Hall and zero-field kinked magnetization measured via vibrating sample magnetometry (VSM, Fig. 3b) is known to be resultant from the interface strain modulated competition of two channels with different Berry curvatures (that dictate the intrinsic  $\rho_{yx}^{\text{AH}}$ ) and magnetic anisotropies [18].

The  $\text{Cr}_2\text{Te}_3$  films have magnetic layers with different anisotropies, as corroborated by the depth-sensitive polarized neutron reflectometry (PNR) investigations performed on a typical  $t = 26$  ML sample at  $T = 100$  K. As shown in Fig. 3c, the depth profile of the nuclear scattering length density (NSLD) is overall uniform, attesting to the high quality and homogeneous distribution across the thickness of the film. The magnetic scattering length density (MSLD) profiles were collected under in-plane (IP) fields of  $\mu_0 H = 1$  T and 0.8 T, then 0.005 T and 0.39 T after sweeping to  $-1$  T. These chosen magnetic fields correspond to the

typical positions in the hysteresis loop as labeled by the asterisks in Fig. 3b. A non-uniform depth-dependent profile with two distinct regions is evident, displaying a lower in-plane magnetization value near the substrate. Considering that the PNR experiments are responsive to the in-plane magnetization vector, the observation indicates the stronger strain at the film/substrate interface induces a higher PMA, and as a result, a lower in-plane MSLD value.

### Monolayer magnetism and its tunability.

VSM measurements were carried out to probe the magnetic ordering of  $\text{Cr}_2\text{Te}_3$ . For 1 ML  $\text{Cr}_2\text{Te}_3$ , the  $Q$  factor (defined as the ratio of the uniaxial anisotropy  $K_u$  and the shape anisotropy  $K_d = 2\pi M^2$ ) is  $\sim 1$  by comparing the hysteresis loops under out-of-plane (OOP) and in-plane field sweeps in Fig. 4a. This indicates comparable out-of-plane and in-plane anisotropies for  $t = 1$  ML in the 2D limit. For 1 ML  $\text{Cr}_2\text{Te}_3$ , it is estimated that  $T_C = 17 (\pm 3)$  K, as judged from the onset in the field-cooled (FC)  $M(T)$  curves in Fig. 5c.

PNR was invoked to examine the ferromagnetism of  $\text{Cr}_2\text{Te}_3$  ultrathin films in the ML regime. The depth-sensitive PNR experiments were carried out on a 2 ML  $\text{Cr}_2\text{Te}_3$  sample, where this thicker  $t$  was chosen and necessary for better signal counts. The spin asymmetry (SA) ratio  $= (R^+ - R^-)/(R^+ + R^-)$  was measured as a function of the wave vector transfer  $Q = 4\pi \sin(\theta)/\lambda$ , where  $R^+$  and  $R^-$  are the reflectivity for the neutron spin parallel (+) or antiparallel (−) to the applied magnetic field, respectively. As shown in Fig. 4b, the non-zero SA substantiates the emergence of magnetization. By refining the PNR data, the depth profiles of NSLD and MSLD were obtained and are depicted in Fig. 4c. The small yet clear presence of the MSLD profile with measured  $M = 37 \text{ emu cm}^{-3}$  at  $T = 5$  K with in-plane  $\mu_0 H = 1$  T reveals the high quality of the magnetic  $\text{Cr}_2\text{Te}_3$  ultrathin films in the ML regime with well-resolved interfacial roughness on the order of 0.5 nm.

To further investigate the magnetism, especially pertaining to transport of 1 ML  $\text{Cr}_2\text{Te}_3$ , temperature dependent AHE transport experiments were performed in the 4 QL BST/1 ML  $\text{Cr}_2\text{Te}_3/\text{SrTiO}_3(111)$  film (1 ML\*). As compiled in Fig. 5b, the AHE hysteresis loop becomes stronger towards lower temperature, indicating the TI layer is exchange proximitized by the 1 ML  $\text{Cr}_2\text{Te}_3$  layer underneath that is ferromagnetic. A large AHE sheet resistivity  $\rho_{yx,\text{sheet}}^{\text{AH}}$  ( $= 117 \Omega$ ) was observed in the film. In turn, as schematically shown in Fig. 5a, the interfacial hybridization with the topological surface states of the TI further strengthens the magnetic ordering in 1 ML  $\text{Cr}_2\text{Te}_3$ , similarly as Katmis *et al.* reported for the EuS/ $\text{Bi}_2\text{Se}_3$  system [31–33].

Accordingly, as summarized in Fig. 5d, the temperature dependences of  $\rho_{yx,\text{sheet}}^{\text{AH}}$  and  $H_c$  uncover the strengthened magnetism with an enhanced  $T_C =$

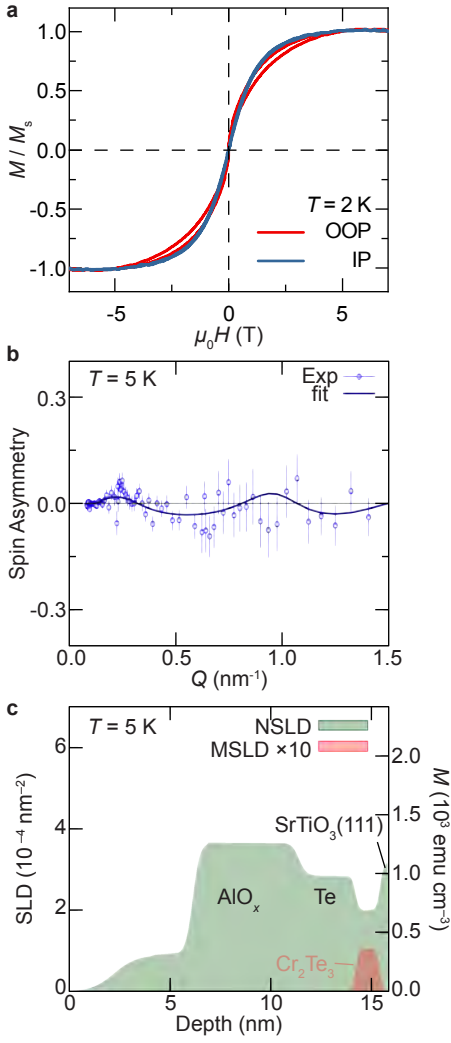


**Figure 4 | Ferromagnetism of  $\text{Cr}_2\text{Te}_3$  films in the monolayer regime.** **a** Field dependent magnetization of 1 ML  $\text{Cr}_2\text{Te}_3$  under out-of-plane (OOP) and in-plane (IP) configurations, respectively. **b** PNR spin asymmetry ratio  $\text{SA} = (R^+ - R^-)/(R^+ + R^-)$  at  $T = 5$  K and IP  $\mu_0 H = 1$  T. **c** Depth profiles of PNR nuclear (NSLD) and magnetic (MSLD, with IP  $\mu_0 H = 1$  T at 5 K) scattering length densities of 2 ML  $\text{Cr}_2\text{Te}_3$  on  $\text{SrTiO}_3(111)$  substrate with  $\text{Te}/\text{AlO}_x$  capping.

$30 (\pm 3)$  K for the 1 ML  $\text{Cr}_2\text{Te}_3$  in the bilayer system. Further control experiments carried out on 2 ML  $\text{Cr}_2\text{Te}_3$  substantiate the effectiveness and robustness of the proximity exchange enhanced ferromagnetism when coupled with a TI. As shown in Fig. 5e-h, the hysteresis loops of 2 ML  $\text{Cr}_2\text{Te}_3$  manifest a  $T_C = 65 (\pm 5)$  K, while enhanced ferromagnetism with a higher  $T_C = 82 (\pm 5)$  K is achieved when heterostructured with the 4 QL BST.

These experimental observations collectively suggest that atomically thin  $\text{Cr}_2\text{Te}_3$  layers as an appealing ferromagnetic insulator candidate, displaying interface tunable 2D magnetism suitable for implementing exchange-coupled vdW spintronics.

### Topological surface-mediated exchange coupling.

To gain insight into magnetic ordering at the  $\text{Cr}_2\text{Te}_3/\text{TI}$  interface, the enhancement of  $T_C$  and PMA, we construct a model Hamiltonian  $H = H_0 + H_{\text{int}}$ , where  $H_0$  is the kinetic energy of electrons in the 2D topological surface states of the 3D TI (BST), and  $H_{\text{int}}$  is the Kondo or  $s$ - $d$  interaction between these electrons and localized Cr moments in  $\text{Cr}_2\text{Te}_3$  at the interface.

The Dirac Hamiltonian  $H_0 = \sum_{\mathbf{k}, \lambda, \lambda'} \hat{c}_{\mathbf{k}\lambda}^\dagger [\hbar v_F (\mathbf{k} \times \boldsymbol{\sigma}^{\lambda\lambda'}) \cdot \hat{\mathbf{z}} + \Delta \sigma_z^{\lambda\lambda'}] \hat{c}_{\mathbf{k}\lambda'}$  describes the surface state electrons on energy scales less than the bandwidth  $W$ . Here  $v_F$  is the Fermi velocity,  $\mathbf{k}$  is the in-plane momentum,  $\boldsymbol{\sigma}$ 's are the spin Pauli matrices,  $\hat{\mathbf{z}}$  is the unit vector normal to the surface,  $\lambda, \lambda'$  are spin labels, and  $\Delta$  is the exchange gap due to broken time-reversal symmetry at the interface.  $H_{\text{int}} = J_K \sum_{i, \lambda, \lambda'} \mathbf{S}_i \cdot \hat{c}_{i\lambda}^\dagger \boldsymbol{\sigma}^{\lambda\lambda'} \hat{c}_{i\lambda'}$  characterizes the Kondo coupling  $J_K$  (with units of energy  $\times$  area) between a local moment  $\mathbf{S}_i$  at  $\mathbf{R}_i$  and the surface state electron spin.

Our first goal is to obtain the effective Hamiltonian

$$H_{\text{eff}} = -\frac{1}{2} \sum_{ij, \alpha\beta} J_{\alpha\beta}(\mathbf{R}_{ij}) S_i^\alpha S_j^\beta, \quad (1)$$

which describes the topological surface state-mediated exchange coupling  $J_{\alpha\beta}(\mathbf{R}_{ij})$  between the classical spins  $\mathbf{S}_i$ . Here  $\mathbf{R}_{ij} = \mathbf{R}_i - \mathbf{R}_j$  and  $\alpha, \beta$  represent  $x, y, z$  spin components. Using second-order perturbation theory in  $J_K/Wa^2$ , where  $a$  is the lattice constant of Cr ions, we find  $H_{\text{eff}}^{(ij)} = -J_K^2 \sum_{\alpha\beta} \chi_{\alpha\beta}(\mathbf{R}_{ij}) S_{i\alpha} S_{j\beta}$ , where  $\chi_{\alpha\beta}(\mathbf{R}_{ij})$  is the static spin susceptibility of the surface state electrons. At zero temperature [34],  $\chi_{\alpha\beta}(\mathbf{R}_{ij}) = (1/\pi) \text{Im} \int_{-\infty}^{\mu} d\omega \text{Tr}[\sigma_\alpha G(\mathbf{R}_{ij}, \omega) \sigma_\beta G(-\mathbf{R}_{ij}, \omega)]$ , where  $\mu$  is the chemical potential, the trace is over spin, and  $G(\mathbf{R}_{ij}, \omega)$  is the retarded electronic Green's function whose form is known analytically [35, 36]. The integral above can be split into two: the  $\int_{-\infty}^0$  piece describes virtual interband transitions from the filled valence band, while the  $\int_0^{\mu}$  piece arises from the Fermi surface of the partially filled conduction band. The latter leads to an oscillatory Ruderman-Kittel-Kasuya-Yosida (RKKY) coupling  $\sim \cos(2k_F R)/R^2$  for  $k_F R \gg 1$ , where  $k_F$  is the Fermi wave vector [37, 38].

The first piece, the Bloembergen-Rowland (BR) interaction [39], is ferromagnetic and decays as  $1/R^3$  for  $a \leq R \ll \hbar v_F/\Delta$  and exponentially for  $R \gg \hbar v_F/\Delta$ . We find [36] that the BR contribution dominates over the RKKY contribution on the distance scale of  $R \sim a$  when we are in the low-doping regime  $k_F a \ll 1$ . We thus neglect the RKKY term and keep the dominant BR coupling.

For simplicity, we assume that the Cr1 and Cr2 sites are the same and this results in a triangular lattice of Cr local moments. We now use the effective Hamiltonian (1) describing spins on a triangular lattice to analyze its properties using several different methods [36].

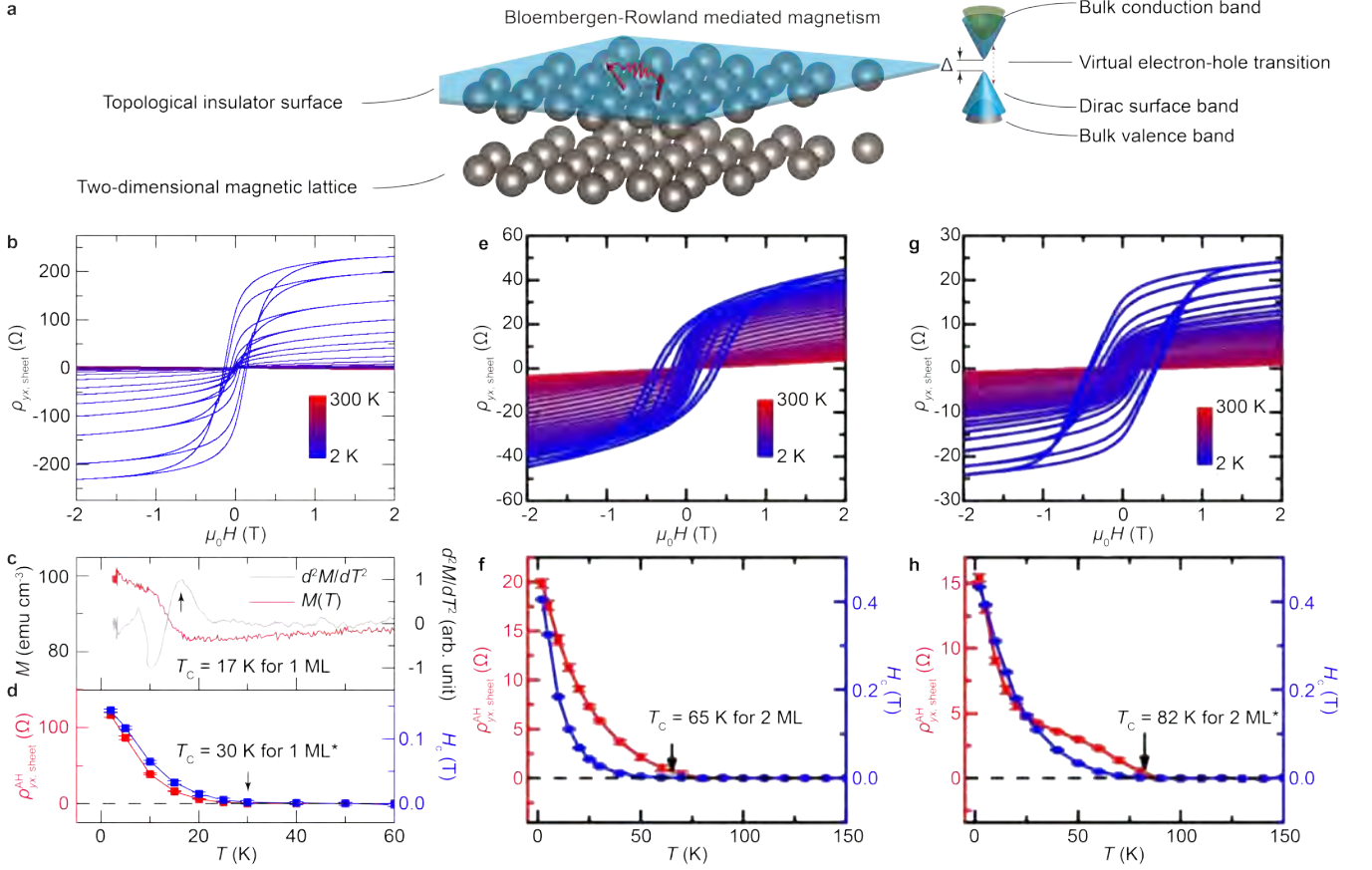


**Figure 5 | Topological surface mediated ferromagnetism of  $\text{Cr}_2\text{Te}_3$  in the monolayer regime.** **a** Enhancing 2D magnetism via the Bloembergen-Rowland interaction in proximity with a topological insulator. **b** Hall traces of 1 ML\*  $\text{Cr}_2\text{Te}_3$  at different temperatures from 2 to 300 K. **c-d** Curie temperature  $T_C$  determined from the magnetization profile of pristine 1 ML  $\text{Cr}_2\text{Te}_3$  film (**c**) and transport data of 1 ML\*  $\text{Cr}_2\text{Te}_3$ /4 QL TI (**d**), namely the anomalous Hall sheet resistance (red) and the coercive field (blue) extracted from **b**. **e,g** Hall traces of 2 ML  $\text{Cr}_2\text{Te}_3$  (**e**) and 4 QL BST/2 ML  $\text{Cr}_2\text{Te}_3$  (**g**, designated as 2 ML\*) at various temperatures. **f,h** Temperature dependence of the anomalous Hall resistance (red) and coercive field (blue) of 2 ML  $\text{Cr}_2\text{Te}_3$  (**f**) and 4 QL BST/2 ML  $\text{Cr}_2\text{Te}_3$  (**h**), where TI-induced enhancement in  $T_C$  of  $\text{Cr}_2\text{Te}_3$  is evident.

First, we show that for small clusters of spins, the ground state is ferromagnetic in OOP direction. Next, by computing the spin-wave spectrum in the full lattice model, we found that the spectrum is gapped and of the form  $\omega(q) = K + Aq^2$  near  $q = 0$ . Here  $A > 0$  is the ferromagnetic exchange stiffness while the gap at  $q = 0$  indicates a PMA of the form  $K = f(a\Delta/\hbar v_F)J_K^2 S/\hbar v_F a^3$ . We find numerically that the dimensionless function  $f \approx 0.15$  when  $a\Delta/\hbar v_F$  lies in the realistic range  $0 - 0.1$ . The magnetic anisotropy arises from the anisotropic nature of the BR interaction, which in turn results from the spin-momentum locking of the surface states [40]. The exchange and PMA stabilize an OOP ferromagnetic order at the interface.

We next perform a mean-field calculation for the full lattice Hamiltonian (1), which leads to  $T_C = [J_K^2 S(S+1)/3k_B] \sum_{\mathbf{R}} \chi_{zz}(\mathbf{R})$  that is proportional to Van Vleck susceptibility. Using parameters relevant

to the  $\text{Cr}_2\text{Te}_3$ /BST system [37, 38, 41]:  $S = 3/2$ ,  $a = 3.93 \text{ \AA}$ ,  $v_F = 3.69 \times 10^5 \text{ m s}^{-1}$ ,  $J_K \approx 1 \text{ eV} \cdot \text{\AA}^2$ , and  $\Delta(T \rightarrow T_C) \rightarrow 0$ , we find  $T_C \approx 23 \text{ K}$ . We note that this is the  $T_C$  enhancement arising from the BR interaction. Given the simplicity of our modeling, this result is in reasonable agreement with our experiments. The theoretical framework we have developed should also be applicable to other examples of  $T_C$  enhancement in TI-proximitized magnets, such as  $\text{Cr}_2\text{Ge}_2\text{Te}_6$  (61 K to 108 K) [42] and  $\text{Fe}_3\text{GeTe}_2$  (230 K to 400 K) [43].

## Conclusion.

The observation of 2D ferromagnetism in monolayer-thick  $\text{Cr}_2\text{Te}_3$  MBE films on insulating  $\text{SrTiO}_3(111)$  substrates has uncovered a novel atomically thin ferromagnetic insulator candidate capable of strong proximity exchange coupling with other vdW quantum materials such as TI for tunable long range order. In particular, via

the BR interaction prevalent when coupling TI to 2D magnets, our comprehensive experimental and theoretical results identify topological surface state proximity as a highly versatile pathway enhancing  $T_C$  in a wide family of 2D magnets. The interface modulated 2D ferromagnetism in  $\text{Cr}_2\text{Te}_3$  and related magnetic TMC films bodes well for future magnetic topological device design towards all-vdW [44] and molecular [45] spintronics.

## METHODS

**Sample growth.** The samples were grown in an ultra-high vacuum (UHV) MBE system with a base pressure  $< 3.7 \times 10^{-10}$  Torr. The growth was monitored by a RHEED system (STAIB 20) with an electron energy of 15 keV. The  $\text{SrTiO}_3(111)$  substrate was rinsed in distilled water at 80 °C for 90 minutes and then annealed in a tube furnace at 950 °C with oxygen flow for 3 hours. Before film growth, the substrate was degassed at 500 °C for 10 min and then heated at 600 °C for 25 min in the MBE chamber. High purity Bi (99.999%), Sb (99.9999%), Te (99.999%), and Cr (99.999%) were co-evaporated from Knudsen cell evaporators and/or e-guns. The flux of each element was monitored by individual quartz crystal monitor during the growth. The growth of  $\text{Cr}_2\text{Te}_3$  was conducted under Te-rich conditions at a substrate temperature of 235 °C with a typical Te/Cr flux ratio of 10. The BST films were grown under the same Te-rich conditions at a substrate temperature of 235 °C with a typical Te/Bi,Sb flux ratio of 10. The Bi/Sb ratio was picked to optimize the resultant chemical potential into the bulk band gap. A 2 nm Te layer and a subsequent 10 nm  $\text{AlO}_x$  layer were *in situ* deposited on the films at room temperature to protect the film from possible degradation by air exposure.

**Raman spectroscopy.** The samples for Raman spectroscopy were capped with *in situ* grown 10 nm  $\text{AlO}_x$ . Raman scattering was performed with a custom built, low temperature microscopy setup [46], using a 532 nm excitation laser that has a spot size of 2  $\mu\text{m}$  in diameter. The spectrometer has a 2400  $\text{g mm}^{-1}$  grating, with an Andor CCD, providing a resolution of  $\sim 1 \text{ cm}^{-1}$ . All data presented in this work were taken at room temperature, and laser heating was minimized using the Stokes to anti-Stokes ratio [47]. Polarization dependence was accomplished by linearly polarizing the excitation laser in the sample plane and rotating the polarization direction via a  $\lambda/2$  Fresnel rhomb. A second polarizer was used to analyze the scattered light, which was either parallel (XX) or perpendicular (XY) to the incoming polarization direction. Dark counts were removed by subtracting data collected with the same integration time with the laser blocked. Furthermore, a recently developed wavelet-based approach was employed to remove the effect of cosmic Rays [48].

**X-ray characterizations.** The XRD patterns were obtained using a parallel beam of  $\text{Cu K}_{\alpha 1}$  radiation with wavelength  $\lambda = 0.15406 \text{ nm}$  in a Rigaku SmartLab system. The  $2\theta$  (for OOP measurement) and/or  $2\theta_\chi$  (for IP configuration) scan angles were typically between 10° and 120° with a step size of 0.05°. XRR measurements were performed at the Center for Nanophase Materials Sciences (CNMS), Oak Ridge National Laboratory, on a PANalytical X'Pert Pro MRD equipped with hybrid monochromator and Xe proportional counter. For the XRR measurements, the X-ray beam was generated at 45 kV/40 mA, and the X-ray beam wavelength after the hybrid mirror was  $\lambda = 0.15406 \text{ nm}$  ( $\text{Cu K}_{\alpha 1}$  radiation).

**Scanning transmission electron microscopy.** STEM experiments were conducted at a probe-corrected STEM (JEOL ARM) operated at an acceleration voltage of 200 kV. Samples were prepared by a Helios focused-ion beam (FEI), operated at an acceleration voltage of 30 kV for the gallium beam during lift-out and of 2 kV during polishing. Additional polishing was performed at 1 kV and 0.5 kV with a NanoMill (Fischione). At both acceleration voltages, samples were polished for 20 min on each side.

**Transport and magnetic measurement.** Transport measurements were performed in a Quantum Design Physical Property Measurement System (PPMS, 1.9 K, 14 T). The film was manually scratched into a Hall bar geometry. The electrodes were made by mechanically pressing fine indium pieces onto the contact areas of the film. The typical sample size was 500  $\mu\text{m} \times 200 \mu\text{m}$ . Magnetic properties were measured in a Quantum Design Magnetic Property Measurement System 3 (MPMS3, 1.8 K, 7 T). The typical sample size was 5 mm  $\times$  5 mm.

**Magnetic force microscopy.** The MFM experiments were carried out in a homemade cryogenic atomic force microscope (AFM) using commercial piezoresistive cantilevers (spring constant  $k \approx 3 \text{ N m}^{-1}$ , resonant frequency  $f_0 \approx 42 \text{ kHz}$ ). The homemade AFM is interfaced with a Nanonis SPM Controller using a phase-lock loop (SPECS). MFM tips were prepared by depositing a 150 nm Co film onto bare tips using electron-beam evaporation. MFM images were taken in a constant height mode with the scanning plane  $\sim 20 \text{ nm}$  above sample surface. The MFM signal, the change of the cantilever resonant frequency  $\delta f$ , is proportional to the OOP force gradient acting on the tip, which is a second derivative of the stray field.

**Polarized neutron reflectometry.** PNR is a highly penetrating depth-sensitive technique to probe the chemical and magnetic depth profiles with a resolution of 0.5 nm. The depth profiles of the NSLD and MSLD correspond to the depth profile of the chemical and IP magnetization vector distributions on the atomic scale, respectively [49–51]. Based on these neutron scattering merits, PNR serves as a powerful technique to simultaneously and nondestructively characterize chemical and

magnetic nature of buried interfaces [52]. PNR experiments were performed on the Magnetism Reflectometer at the Spallation Neutron Source at Oak Ridge National Laboratory [53–56], using neutrons with wavelengths  $\lambda$  in a band of 0.2–0.8 nm and a high polarization of 98.5–99%. Measurements were conducted in a closed cycle refrigerator (Advanced Research System) equipped with a 1.15 T electromagnet (Bruker). Using the time-of-flight method, a collimated polychromatic beam of polarized neutrons with the wavelength band  $\delta\lambda$  impinged on the film at a grazing angle  $\theta$ , interacting with atomic nuclei and the spins of unpaired electrons. The reflected intensity  $R^+$  and  $R^-$  were measured as a function of momentum transfer,  $Q = 4\pi \sin(\theta)/\lambda$ , with the neutron spin parallel (+) or antiparallel (–), respectively, to the applied field. To separate the nuclear from the magnetic scattering, the spin asymmetry ratio  $SA = (R^+ - R^-)/(R^+ + R^-)$  was calculated, with  $SA = 0$  designating no magnetic moment in the system. Being electrically neutral, spin-polarized neutrons penetrate the entire multilayer structures and probe magnetic and structural composition of the film and buried interfaces down to the substrate.

**Data availability.** The data that support the findings of this study are available from the corresponding authors upon reasonable request.

## ACKNOWLEDGMENTS

This work was supported by Army Research Office (ARO W911NF-20-2-0061), the National Science Foundation (NSF-DMR 2218550), Office of Naval Research (N00014-20-1-2306). H.C. was sponsored by the Army Research Laboratory under Cooperative Agreement Number W911NF-19-2-0015 and acknowledges the start-up fund at the University of Ottawa. Y.O., D.S., J.S.M. and D.C.B. thank the Center for Integrated Quantum Materials (NSF-DMR 1231319) for financial support. This work made use of the MIT Materials Research Laboratory. D.H. thanks support from NSF-DMR 1905662 and the Air Force Office of Scientific Research Award No. FA9550-20-1-0247. N.M.N. and J.L.M. were supported by Ministerio de Ciencia e Innovacion, Spain, with grant numbers MAT2017-84496-R, PID2021-122477OB-I00, TED2021-129254B-C21 and TED2021-129254B-C22. M.R. received funding from the European Union Horizon 2020 research and innovation programme under the Marie Skłodowska-Curie grant agreement Eu-Super No. 796603. The STEM work was performed in part at the Center for Nanoscale Systems (CNS), a member of the National Nanotechnology Coordinated Infrastructure Network (NNCI), which is supported by NSF Award No. 1541959. The MFM studies at Rutgers were supported by the Office of Basic Energy Sciences, Division of Materials Sciences and Engineering, U.S. Department of Energy under Award No. DE-SC0018153. Y.W.

and K.S.B. are grateful for the primary support of the US Department of Energy, Office of Science, Office of Basic Energy Sciences under award no. DE-SC0018675. This research used resources at the Spallation Neutron Source, a Department of Energy Office of Science User Facility operated by the Oak Ridge National Laboratory (ORNL). XRR measurements were conducted at the Center for Nanophase Materials Sciences (CNMS) at ORNL, which is a DOE Office of Science User Facility. M.M., M.Ra. and N.T. were supported by the NSF Materials Research Science and Engineering Center Grant No. DMR-2011876. N.T. thanks K. Lee for discussions.

## AUTHOR CONTRIBUTIONS

Y.O., J.S.M. and H.C. conceived the project. The samples were prepared and characterized by Y.O. and H.C.. N.M.N., J.L.M., M.Ro., Y.O. and H.C. performed transport measurements. Y.O., H.C. and D.H. carried out magnetization measurements. A.A. and D.C.B. collected HRSTEM images. W.G. and W.W. obtained MFM images. D.S., Y.W. and K.S.B. performed Raman measurements. J.K. performed XRR measurements, V.L. and H.A. conducted PNR experiments, V.L. analyzed XRR and PNR data. M.M., M.Ra. and N.T. provided theoretical modeling and analysis. Y.O., J.S.M. and H.C. wrote the paper with input from all authors. All authors discussed the results.

---

\* [ybou@mit.edu](mailto:ybou@mit.edu)

† [moodera@mit.edu](mailto:moodera@mit.edu)

‡ [hang.chi@uottawa.ca](mailto:hang.chi@uottawa.ca)

- [1] H. Yang, S. O. Valenzuela, M. Chshiev, S. Couet, B. Diny, B. Dlubak, A. Fert, K. Garello, M. Jamet, D.-E. Jeong, K. Lee, T. Lee, M.-B. Martin, G. S. Kar, P. S enior, H.-J. Shin, and S. Roche, Two-dimensional materials prospects for non-volatile spintronic memories, *Nature* **606**, 663 (2022).
- [2] K. S. Burch, D. Mandrus, and J.-G. Park, Magnetism in two-dimensional van der Waals materials, *Nature* **563**, 47 (2018).
- [3] C. Gong and X. Zhang, Two-dimensional magnetic crystals and emergent heterostructure devices, *Science* **363**, eaav4450 (2019).
- [4] M. Gibertini, M. Koperski, A. F. Morpurgo, and K. S. Novoselov, Magnetic 2D materials and heterostructures, *Nature Nanotechnology* **14**, 408 (2019).
- [5] K. F. Mak, J. Shan, and D. C. Ralph, Probing and controlling magnetic states in 2D layered magnetic materials, *Nature Reviews Physics* **1**, 646 (2019).
- [6] J.-U. Lee, S. Lee, J. H. Ryoo, S. Kang, T. Y. Kim, P. Kim, C.-H. Park, J.-G. Park, and H. Cheong, Ising-Type Magnetic Ordering in Atomically Thin FePS<sub>3</sub>, *Nano Letters* **16**, 7433 (2016).

- [7] B. Huang, G. Clark, E. Navarro-Moratalla, D. R. Klein, R. Cheng, K. L. Seyler, D. Zhong, E. Schmidgall, M. A. McGuire, D. H. Cobden, W. Yao, D. Xiao, P. Jarillo-Herrero, and X. Xu, Layer-dependent ferromagnetism in a van der Waals crystal down to the monolayer limit, *Nature* **546**, 270 (2017).
- [8] C. Gong, L. Li, Z. Li, H. Ji, A. Stern, Y. Xia, T. Cao, W. Bao, C. Wang, Y. Wang, Z. Q. Qiu, R. J. Cava, S. G. Louie, J. Xia, and X. Zhang, Discovery of intrinsic ferromagnetism in two-dimensional van der Waals crystals, *Nature* **546**, 265 (2017).
- [9] Y. Deng, Y. Yu, Y. Song, J. Zhang, N. Z. Wang, Z. Sun, Y. Yi, Y. Z. Wu, S. Wu, J. Zhu, J. Wang, X. H. Chen, and Y. Zhang, Gate-tunable room-temperature ferromagnetism in two-dimensional  $\text{Fe}_3\text{GeTe}_2$ , *Nature* **563**, 94 (2018).
- [10] M. Bonilla, S. Kolekar, Y. Ma, H. C. Diaz, V. Kalappattil, R. Das, T. Eggers, H. R. Gutierrez, M.-H. Phan, and M. Batzill, Strong room-temperature ferromagnetism in  $\text{VSe}_2$  monolayers on van der Waals substrates, *Nature Nanotechnology* **13**, 289 (2018).
- [11] D. J. O'Hara, T. Zhu, A. H. Trout, A. S. Ahmed, Y. K. Luo, C. H. Lee, M. R. Brenner, S. Rajan, J. A. Gupta, D. W. McComb, and R. K. Kawakami, Room Temperature Intrinsic Ferromagnetism in Epitaxial Manganese Selenide Films in the Monolayer Limit, *Nano Letters* **18**, 3125 (2018).
- [12] E. J. Telford, A. H. Dismukes, K. Lee, M. Cheng, A. Wieteska, A. K. Bartholomew, Y.-S. Chen, X. Xu, A. N. Pasupathy, X. Zhu, C. R. Dean, and X. Roy, Layered Antiferromagnetism Induces Large Negative Magnetoresistance in the van der Waals Semiconductor  $\text{CrSb}$ , *Advanced Materials* **32**, 2003240 (2020).
- [13] J. Klein, Z. Song, B. Pingault, F. Dirnberger, H. Chi, J. B. Curtis, R. Dana, R. Bushati, J. Quan, L. Dekanovsky, Z. Sofer, A. Al, V. M. Menon, J. S. Moodera, M. Lonar, P. Narang, and F. M. Ross, Sensing the Local Magnetic Environment through Optically Active Defects in a Layered Magnetic Semiconductor, *ACS Nano* **17**, 288 (2023).
- [14] E. Park, J. P. Philbin, H. Chi, J. J. Sanchez, C. Occhialini, G. Varnavides, J. B. Curtis, Z. Song, J. P. Klein, J. D. Thomsen, M.-G. Han, A. C. Foucher, K. Mosina, D. Kumawat, N. Gonzalez-Yepepe, Y. Zhu, Z. Sofer, R. Comin, J. S. Moodera, P. Narang, and F. M. Ross, Atomistic Characterization and Engineering of Anisotropic 2D van der Waals Magnets Hosting 1D Spin Chains, *Nature Materials*, submitted (2023).
- [15] K. Kim, J. Seo, E. Lee, K. T. Ko, B. S. Kim, B. G. Jang, J. M. Ok, J. Lee, Y. J. Jo, W. Kang, J. H. Shim, C. Kim, H. W. Yeom, B. Il Min, B.-J. Yang, and J. S. Kim, Large anomalous Hall current induced by topological nodal lines in a ferromagnetic van der Waals semimetal, *Nature Materials* **17**, 794 (2018).
- [16] Y. Wu, B. Francisco, Z. Chen, W. Wang, Y. Zhang, C. Wan, X. Han, H. Chi, Y. Hou, A. Lodesani, G. Yin, K. Liu, Y.-T. Cui, K. L. Wang, and J. S. Moodera, A Van der Waals Interface Hosting Two Groups of Magnetic Skyrmions, *Advanced Materials* **34**, 2110583 (2022).
- [17] T. Song, X. Cai, M. W.-Y. Tu, X. Zhang, B. Huang, N. P. Wilson, K. L. Seyler, L. Zhu, T. Taniguchi, K. Watanabe, M. A. McGuire, D. H. Cobden, D. Xiao, W. Yao, and X. Xu, Giant tunneling magnetoresistance in spin-filter van der Waals heterostructures, *Science* **360**, 1214 (2018).
- [18] H. Chi, Y. Ou, T. B. Eldred, W. Gao, S. Kwon, J. Murray, M. Dreyer, R. E. Butera, A. C. Foucher, H. Ambaye, J. Keum, A. T. Greenberg, Y. Liu, M. R. Neupane, G. J. de Coster, O. A. Vail, P. J. Taylor, P. A. Folkes, C. Rong, G. Yin, R. K. Lake, F. M. Ross, V. Lauter, D. Heiman, and J. S. Moodera, Strain-tunable Berry curvature in quasi-two-dimensional chromium telluride, *Nature Communications* **14**, 3222 (2023).
- [19] Y. Zhong, C. Peng, H. Huang, D. Guan, J. Hwang, K. H. Hsu, Y. Hu, C. Jia, B. Moritz, D. Lu, J.-S. Lee, J.-F. Jia, T. P. Devereaux, S.-K. Mo, and Z.-X. Shen, From Stoner to local moment magnetism in atomically thin  $\text{Cr}_2\text{Te}_3$ , *Nature Communications* **14**, 5340 (2023).
- [20] H. Chi and J. S. Moodera, Progress and prospects in the quantum anomalous Hall effect, *APL Materials* **10**, 090903 (2022).
- [21] M. Yuzuri, T. Kanomata, and T. Kaneko, The pressure effect on the Curie temperature and exchange striction of  $\text{Cr}_2\text{S}_3$  and  $\text{Cr}_2\text{Te}_3$ , *Journal of Magnetism and Magnetic Materials* **70**, 223 (1987).
- [22] D. C. Freitas, R. Weht, A. Sulpice, G. Remenyi, P. Strobel, F. Gay, J. Marcus, and M. Nez-Regueiro, Ferromagnetism in layered metastable 1T- $\text{CrTe}_2$ , *Journal of Physics: Condensed Matter* **27**, 176002 (2015).
- [23] L. Meng, Z. Zhou, M. Xu, S. Yang, K. Si, L. Liu, X. Wang, H. Jiang, B. Li, P. Qin, P. Zhang, J. Wang, Z. Liu, P. Tang, Y. Ye, W. Zhou, L. Bao, H.-J. Gao, and Y. Gong, Anomalous thickness dependence of Curie temperature in air-stable two-dimensional ferromagnetic 1T- $\text{CrTe}_2$  grown by chemical vapor deposition, *Nature Communications* **12**, 809 (2021).
- [24] X. Zhang, Q. Lu, W. Liu, W. Niu, J. Sun, J. Cook, M. Vaninger, P. F. Miceli, D. J. Singh, S.-W. Lian, T.-R. Chang, X. He, J. Du, L. He, R. Zhang, G. Bian, and Y. Xu, Room-temperature intrinsic ferromagnetism in epitaxial  $\text{CrTe}_2$  ultrathin films, *Nature Communications* **12**, 2492 (2021).
- [25] Y. Ou, W. Yanez, R. Xiao, M. Stanley, S. Ghosh, B. Zheng, W. Jiang, Y.-S. Huang, T. Pillsbury, A. Richardella, C. Liu, T. Low, V. H. Crespi, K. A. Mkhoyan, and N. Samarth,  $\text{ZrTe}_2/\text{CrTe}_2$ : an epitaxial van der Waals platform for spintronics, *Nature Communications* **13**, 2972 (2022).
- [26] T. Hamasaki, T. Hashimoto, Y. Yamaguchi, and H. Watanabe, Neutron diffraction study of  $\text{Cr}_2\text{Te}_3$  single crystal, *Solid State Communications* **16**, 895 (1975).
- [27] M. Bester, I. Stefaniuk, and M. Kuzma, Quasi-Two-Dimensional Ferromagnetism in  $\text{Cr}_2\text{Te}_3$  and  $\text{Cr}_5\text{Te}_8$  Crystals, *Acta Physica Polonica A* **127**, 433 (2015).
- [28] A. Roy, S. Guchhait, R. Dey, T. Pramanik, C.-C. Hsieh, A. Rai, and S. K. Banerjee, Perpendicular Magnetic Anisotropy and Spin Glass-like Behavior in Molecular Beam Epitaxy Grown Chromium Telluride Thin Films, *ACS Nano* **9**, 3772 (2015).
- [29] J. Chen, L. Wang, M. Zhang, L. Zhou, R. Zhang, L. Jin, X. Wang, H. Qin, Y. Qiu, J. Mei, F. Ye, B. Xi, H. He, B. Li, and G. Wang, Evidence for Magnetic Skyrmions at the Interface of Ferromagnet/Topological-Insulator Heterostructures, *Nano Letters* **19**, 6144 (2019).
- [30] Q. Guillet, L. Vojáček, D. Dosenovic, F. Ibrahim, H. Boukari, J. Li, F. Choueikani, P. Ohresser, A. Ouerghi, F. Mesple, V. Renard, J.-F. Jacquot, D. Jalabert, H. Okuno, M. Chshiev, C. Vergnaud, F. Bonell, A. Marty,



- and M. Jamet, Epitaxial van der Waals heterostructures of  $\text{Cr}_2\text{Te}_3$  on two-dimensional materials, *Physical Review Materials* **7**, 054005 (2023).
- [31] F. Katmis, V. Lauter, F. S. Nogueira, B. A. Assaf, M. E. Jamer, P. Wei, B. Satpati, J. W. Freeland, I. Eremin, D. Heiman, P. Jarillo-Herrero, and J. S. Moodera, A high-temperature ferromagnetic topological insulating phase by proximity coupling, *Nature* **533**, 513 (2016).
- [32] C. Lee, F. Katmis, P. Jarillo-Herrero, J. S. Moodera, and N. Gedik, Direct measurement of proximity-induced magnetism at the interface between a topological insulator and a ferromagnet, *Nature Communications* **7**, 12014 (2016).
- [33] G. B. Osterhoudt, R. Carelli, K. S. Burch, F. Katmis, N. Gedik, and J. S. Moodera, Charge transfer in  $\text{EuS}/\text{Bi}_2\text{Se}_3$  heterostructures as indicated by the absence of Raman scattering, *Physical Review B* **98**, 014308 (2018).
- [34] H. Imamura, P. Bruno, and Y. Utsumi, Twisted exchange interaction between localized spins embedded in a one- or two-dimensional electron gas with Rashba spin-orbit coupling, *Physical Review B* **69**, 121303 (2004).
- [35] D. K. Efimkin and V. Galitski, Self-consistent theory of ferromagnetism on the surface of a topological insulator, *Physical Review B* **89**, 115431 (2014).
- [36] M. Mirzhalilov, H. Chi, J. S. Moodera, M. Randeria, and N. Trivedi, in preparation.
- [37] J.-J. Zhu, D.-X. Yao, S.-C. Zhang, and K. Chang, Electrically Controllable Surface Magnetism on the Surface of Topological Insulators, *Physical Review Letters* **106**, 097201 (2011).
- [38] Q. Liu, C.-X. Liu, C. Xu, X.-L. Qi, and S.-C. Zhang, Magnetic Impurities on the Surface of a Topological Insulator, *Physical Review Letters* **102**, 156603 (2009).
- [39] N. Bloembergen and T. J. Rowland, Nuclear Spin Exchange in Solids:  $\text{Tl}^{203}$  and  $\text{Tl}^{205}$  Magnetic Resonance in Thallium and Thallous Oxide, *Physical Review* **97**, 1679 (1955).
- [40] D. A. Abanin and D. A. Pesin, Ordering of Magnetic Impurities and Tunable Electronic Properties of Topological Insulators, *Physical Review Letters* **106**, 136802 (2011).
- [41] X. He, H. Li, L. Chen, and K. Wu, Substitution-induced spin-split surface states in topological insulator  $(\text{Bi}_{1-x}\text{Sb}_x)_2\text{Te}_3$ , *Scientific Reports* **5**, 8830 (2015).
- [42] L. D. Alegria, H. Ji, N. Yao, J. J. Clarke, R. J. Cava, and J. R. Petta, Large anomalous hall effect in ferromagnetic insulator-topological insulator heterostructures, *Applied Physics Letters* **105**, 053512 (2014).
- [43] H. Wang, Y. Liu, P. Wu, W. Hou, Y. Jiang, X. Li, C. Pandey, D. Chen, Q. Yang, H. Wang, D. Wei, N. Lei, W. Kang, L. Wen, T. Nie, W. Zhao, and K. L. Wang, Above Room-Temperature Ferromagnetism in Wafer-Scale Two-Dimensional van der Waals  $\text{Fe}_3\text{GeTe}_2$  Tailored by a Topological Insulator, *ACS Nano* **14**, 10045 (2020).
- [44] Y. Liu, Y. Huang, and X. Duan, Van der Waals integration before and beyond two-dimensional materials, *Nature* **567**, 323 (2019).
- [45] K. V. Raman, A. M. Kamerbeek, A. Mukherjee, N. Atodiresei, T. K. Sen, P. Lazić, V. Caciuc, R. Michel, D. Stalke, S. K. Mandal, S. Blgel, M. Mnzenberg, and J. S. Moodera, Interface-engineered templates for molecular spin memory devices, *Nature* **493**, 509 (2013).
- [46] Y. Tian, A. A. Reijnders, G. B. Osterhoudt, I. Valmianski, J. G. Ramirez, C. Urban, R. Zhong, J. Schneeloch, G. Gu, I. Henslee, and K. S. Burch, Low vibration high numerical aperture automated variable temperature Raman microscope, *Review of Scientific Instruments* **87**, 043105 (2016).
- [47] Y. Wang, G. B. Osterhoudt, Y. Tian, P. Lampen-Kelley, A. Banerjee, T. Goldstein, J. Yan, J. Knolle, H. Ji, R. J. Cava, J. Nasu, Y. Motome, S. E. Nagler, D. Mandrus, and K. S. Burch, The range of non-Kitaev terms and fractional particles in  $\alpha\text{-RuCl}_3$ , *npj Quantum Materials* **5**, 14 (2020).
- [48] Y. Tian and K. S. Burch, Automatic Spike Removal Algorithm for Raman Spectra, *Applied Spectroscopy* **70**, 1861 (2016).
- [49] S. J. Blundell, M. Gester, J. A. C. Bland, H. J. Lauter, V. V. Pasyuk, and A. V. Petrenko, Spin-orientation dependence in neutron reflection from a single magnetic film, *Physical Review B* **51**, 9395 (1995).
- [50] V. Lauter-Pasyuk, H. J. Lauter, B. Toperverg, O. Nikonov, E. Kravtsov, M. A. Milyaev, L. Romashev, and V. Ustinov, Magnetic off-specular neutron scattering from Fe/Cr multilayers, *Physica B: Condensed Matter* **283**, 194 (2000).
- [51] V. Lauter-Pasyuk, Neutron grazing incidence techniques for nano-science, Collection SFN **7**, s221 (2007).
- [52] V. Lauter, H. J. C. Lauter, A. Glavic, and B. P. Toperverg, Reflectivity, Off-Specular Scattering, and GISANS Neutrons, in *Reference Module in Materials Science and Materials Engineering*, edited by S. Hashmi (Oxford: Elsevier, 2016) pp. 1–27.
- [53] V. Lauter, H. Ambaye, R. Goyette, W.-T. Hal Lee, and A. Parizzi, Highlights from the magnetism reflectometer at the SNS, *Physica B: Condensed Matter* **404**, 2543 (2009).
- [54] X. Tong, C. Y. Jiang, V. Lauter, H. Ambaye, D. Brown, L. Crow, T. R. Gentile, R. Goyette, W. T. Lee, A. Parizzi, and J. L. Robertson, *In situ* polarized  $^3\text{He}$  system for the Magnetism Reflectometer at the Spallation Neutron Source, *Review of Scientific Instruments* **83**, 075101 (2012).
- [55] V. G. Syromyatnikov, V. A. Ulyanov, V. Lauter, V. M. Pusenkov, H. Ambaye, R. Goyette, M. Hoffmann, A. P. Bulkin, I. N. Kuznetsov, and E. N. Medvedev, A new type of wide-angle supermirror analyzer of neutron polarization, *Journal of Physics: Conference Series* **528**, 012021 (2014).
- [56] C. Y. Jiang, X. Tong, D. R. Brown, A. Glavic, H. Ambaye, R. Goyette, M. Hoffmann, A. A. Parizzi, L. Robertson, and V. Lauter, New generation high performance *in situ* polarized  $^3\text{He}$  system for time-of-flight beam at spallation sources, *Review of Scientific Instruments* **88**, 025111 (2017).

# Supplementary Information

## Enhanced Ferromagnetism in Monolayer $\text{Cr}_2\text{Te}_3$ via Topological Insulator Coupling

Yunbo Ou,<sup>1</sup> Murod Mirzhalilov,<sup>2</sup> Norbert M. Nemes,<sup>3</sup> Jose L. Martinez,<sup>4</sup> Mirko Rocci,<sup>1</sup>  
Austin Akey,<sup>5</sup> Wenbo Ge,<sup>6</sup> Dhavala Suri,<sup>7</sup> Yiping Wang,<sup>8</sup> Haile Ambaye,<sup>9</sup> Jong Keum,<sup>9,10</sup>  
Mohit Randeria,<sup>2</sup> Nandini Trivedi,<sup>2</sup> Kenneth S. Burch,<sup>8</sup> David C. Bell,<sup>5</sup> Weida Wu,<sup>6</sup>  
Don Heiman,<sup>1,11</sup> Valeria Lauter,<sup>9</sup> Jagadeesh S. Moodera,<sup>1,12</sup> and Hang Chi<sup>1,13,14</sup>

<sup>1</sup>*Francis Bitter Magnet Laboratory, Plasma Science and Fusion Center,  
Massachusetts Institute of Technology, Cambridge, Massachusetts 02139, USA*

<sup>2</sup>*Department of Physics, The Ohio State University, Columbus, Ohio 43210, USA*

<sup>3</sup>*GFMC, Departamento Física de Materiales. Facultad de Ciencias Físicas,  
Universidad Complutense de Madrid, 28040, Madrid, Spain*

<sup>4</sup>*Instituto de Ciencia de Materiales de Madrid ICMM-CSIC,*

*Calle Sor Juana Inés de la Cruz, 3, Cantoblanco, Madrid 28049, Spain*

<sup>5</sup>*Center for Nanoscale Systems, Harvard University, Massachusetts 02139, USA*

<sup>6</sup>*Department of Physics and Astronomy, Rutgers University, Piscataway, New Jersey 08854, USA*

<sup>7</sup>*Centre for Nano Science and Engineering, Indian Institute of Science, Bengaluru, Karnataka 560012, India*

<sup>8</sup>*Department of Physics, Boston College, Chestnut Hill, Massachusetts 02467, USA*

<sup>9</sup>*Neutron Scattering Division, Neutron Sciences Directorate,*

*Oak Ridge National Laboratory, Oak Ridge, Tennessee 37831, USA*

<sup>10</sup>*Center for Nanophase Materials Sciences, Physical Science Directorate,*

*Oak Ridge National Laboratory, Oak Ridge, Tennessee 37831, USA*

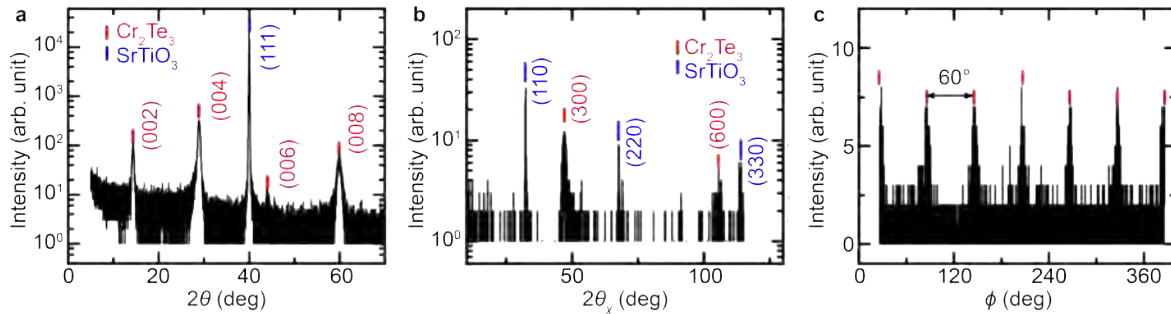
<sup>11</sup>*Department of Physics, Northeastern University, Boston, Massachusetts 02115, USA*

<sup>12</sup>*Department of Physics, Massachusetts Institute of Technology, Cambridge, Massachusetts 02139, USA*

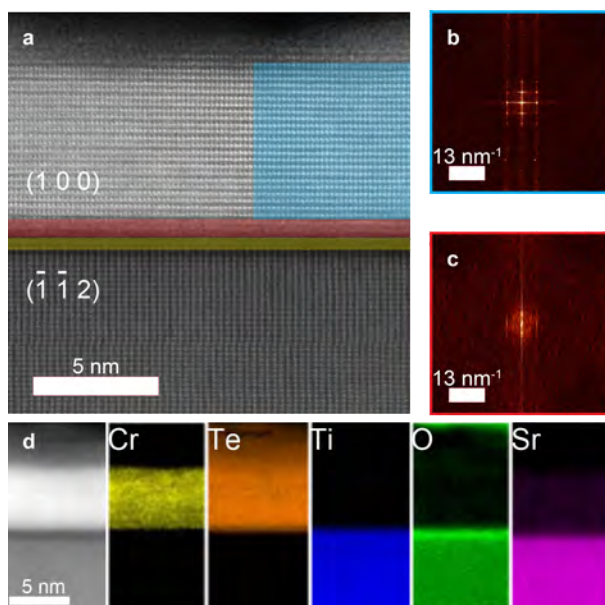
<sup>13</sup>*Department of Physics, University of Ottawa, Ottawa, Ontario K1N 6N5, Canada*

<sup>14</sup>*Nexus for Quantum Technologies, University of Ottawa, Ottawa, Ontario, K1N 6N5, Canada*

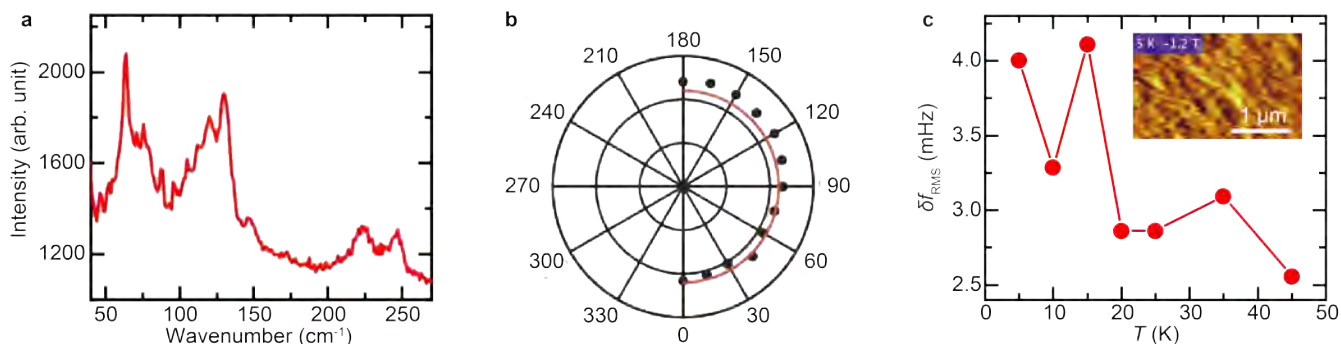
(Dated: December 27, 2023)



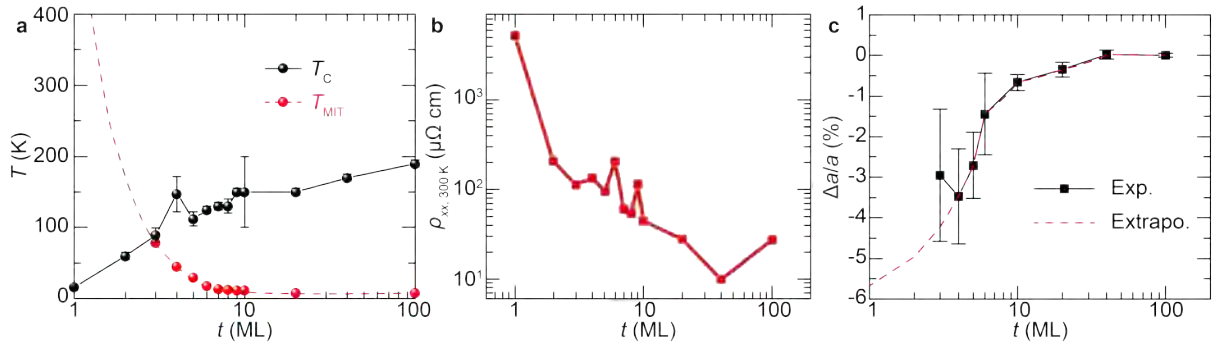
**Supplementary Figure 1 | X-ray diffraction of 20 monolayer  $\text{Cr}_2\text{Te}_3$  film on  $\text{SrTiO}_3(111)$ . Typical out-of-plane XRD  $2\theta$  scan (a), in-plane  $2\theta_\chi$  scan (b) and  $\phi$  scan (c).**



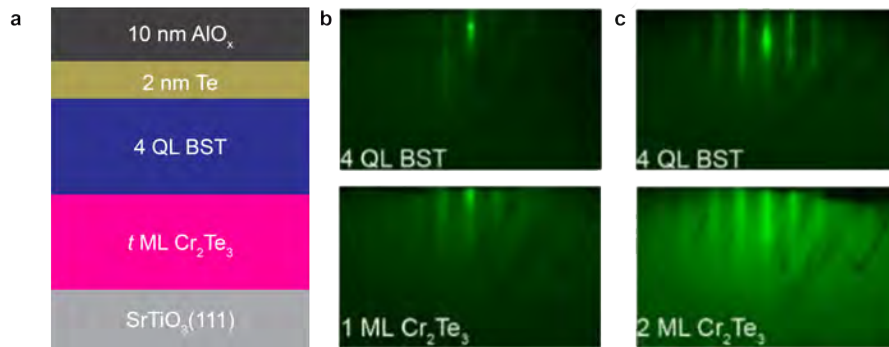
**Supplementary Figure 2 | Scanning transmission electron microscopy of  $\text{Cr}_2\text{Te}_3$  films.** **a** Large scale HRSTEM HAADF image of 13 ML  $\text{Cr}_2\text{Te}_3$  on  $\text{SrTiO}_3$  for the (100) plane. The first ML of  $\text{Cr}_2\text{Te}_3$  on  $\text{SrTiO}_3$  and the  $\text{TiO}_x$  top layer of  $\text{SrTiO}_3$  are indicated by red and yellow. **b-c** FFT of the blue (b) and red (c) regions as indicated in a. **d** HAADF STEM image (left) and the corresponding EDS elemental mapping.



**Supplementary Figure 3 | Raman spectroscopy and magnetic force microscopy of  $\text{Cr}_2\text{Te}_3$  films.** **a** The Raman spectra of  $\text{Cr}_2\text{Te}_3$  with XX polarization at room temperature. **b** The polar plot of a representative phonon mode of  $\text{Cr}_2\text{Te}_3$ . **c** Temperature dependence of the root-mean-square (RMS) value of the MFM signal. The inset is the MFM image scanned at 5 K with a -1.2 T magnetic field applied along the  $c$  direction.



**Supplementary Figure 4 | Thickness dependent physical properties of  $\text{Cr}_2\text{Te}_3$  films.** **a** Thickness dependence of the Curie temperature  $T_C$  and the inflection point  $T_{\text{MIT}}$  in resistivity  $\rho(T)$ , revealing a metal-insulator transition. **b** Layer dependence of the electrical resistivity of  $\text{Cr}_2\text{Te}_3$  films at room temperature. **c** Layer sensitive relative change in the in-plane lattice parameter  $a$ .



**Supplementary Figure 5 | Few layer  $\text{Cr}_2\text{Te}_3$  proximitized with  $(\text{Bi,Sb})_2\text{Te}_3$  topological insulator.** **a** Schematic structure of  $(\text{Bi,Sb})_2\text{Te}_3$  (BST)/ $\text{Cr}_2\text{Te}_3$  heterostructure. **b-c** RHEED patterns of 4 QL BST/1 ML  $\text{Cr}_2\text{Te}_3$  (b) and 4 QL BST/2 ML  $\text{Cr}_2\text{Te}_3$  (c) along the [100] direction of  $\text{Cr}_2\text{Te}_3$ .